AIAA JOURNAL
Vol. 47, No. 11, November 2009

Fatigue Damage Prediction in Metallic Materials Based on Multiscale Modeling

Chuntao Luo,* Jun Wei,† Manuel Parra–Garcia,‡ Aditi Chattopadhyay,§ and Pedro Peralta¶
Arizona State University, Tempe, Arizona 85287

DOI: 10.2514/1.39559

This paper addresses the problem of predicting fatigue damage accumulation in metallic materials accounting for local crystal orientation effects using a multiscale model. Single crystal plasticity is introduced to describe crystalline material behavior. At the mesoscale level, different material properties and crystal orientations are assigned to individual grains in a finite element model. Finally, an average method is used to compute the material properties at the mesoscale, which are then applied to a macroscale representative test structure. To predict fatigue damage evolution, a comprehensive fatigue damage criterion is modified to account for single crystal plasticity.

I. Introduction

HIGH-CYCLE fatigue (HCF) is one of the leading causes of structural failure in aerospace vehicles. Although significant attention has been devoted to this area for many years, prediction of the failure modes associated with HCF still remains a challenging area of research [1]. Unfortunately, traditional life prediction methods are commonly based on the macroscopic response of the material, and the failure laws mostly depend on experimental observations. Because of current industrial and military demands for materials to approach the limit of their capabilities, the use of traditional life prediction methods implies a large amount of data and experiments to support the safe life approach. The rise in costs has prompted the search for more efficient methods to predict fatigue life. From a physical point of view, the repeated variations of elastic stresses in metals induce microinternal stresses above the local yield stress, with dissipation of energy via microplastic strains, which leads to local crystallographic slip due to dislocations glide. Then, there is formation of permanent microslip bands and decohesions, often at the surface of the material, typically linked to the presence of surface roughness in the form of intrusions and extrusions. After this first stage located inside the grains, where the microcracks typically follow the planes of maximum shear strain, there is a second stage in which the microcracks cross the crystal boundaries to grow more or less perpendicular to the direction of the maximum principal stress up to coalescence to produce a mesocrack [2].

The need to predict the evolution of fatigue damage from crack nucleation to long crack propagation requires a physics-based multiscale model for HCF. In this paper, a micro–meso multiscale model that accounts for grain orientation effects is developed to capture the damage initiation and progression due to HCF. To implement the multiscale model into the application for HCF, a corresponding modified fatigue damage criterion is also used.

II. Multiscale Modeling

A. Microscale Model

Single crystal plasticity theory is used to capture crystallographic orientation effects that are not considered by classical isotropic models of metal plasticity. The kinematic theory for single crystal deformation presented here follows the pioneering work of Taylor [3] and its precise mathematical theory by Hill [4], Rice [5], Hill and Rice [6], Asaro and Rice[7], and Asaro [8,9]. Using the standard multiplicative decomposition assumption, the deformation gradient $\mathbf{F} = \partial \mathbf{x} / \partial \mathbf{X}$ can be decomposed into elastic and plastic components as shown in Fig. 1.

$$\mathbf{F} = \mathbf{F}^{\mathbf{e}} \cdot \mathbf{F}^{\mathbf{p}} \tag{1}$$

Here, $\mathbf{F}^{\mathbf{p}}$ denotes plastic deformation of the material in an intermediate configuration in which lattice orientation and spacing remain the same as in the reference configuration. $\mathbf{F}^{\mathbf{e}}$ denotes the elastic component of the deformation gradient, which includes stretching and rotation of the lattice. The velocity gradient, $\mathbf{L} = \partial \mathbf{v} / \partial \mathbf{x}$, in the current configuration is related to the deformation gradient by:

$$\mathbf{L} = \dot{\mathbf{F}}\mathbf{F}^{-1} = \mathbf{L}^{\mathbf{e}} + \mathbf{L}^{\mathbf{p}} \tag{2}$$

where $\mathbf{L}^{\mathbf{e}} = \dot{\mathbf{F}}^{\mathbf{e}}\mathbf{F}^{\mathbf{e}-1}$ and $\mathbf{L}^{\mathbf{p}} = \mathbf{F}^{\mathbf{e}}\dot{\mathbf{F}}^{\mathbf{p}}\mathbf{F}^{\mathbf{p}-1}\mathbf{F}^{\mathbf{e}-1}$ represent the elastic and plastic components of the velocity gradient, respectively.

Assuming that the inelastic deformation of a single crystal arises solely from crystalline slip, the plastic velocity gradient can be rewritten in terms of the resolved slip rate $\dot{\gamma}^{(\alpha)}$, the slip direction $\mathbf{s}^{(\ddagger)}$, and the normal $\mathbf{m}^{(\ddagger)}$ to the slip plane as follows:

$$L^p = \sum_{\alpha} \dot{\gamma}^{(\alpha)} \mathbf{s}^{(\boldsymbol{\alpha})} \otimes \mathbf{m}^{(\boldsymbol{\alpha})} \tag{3}$$

where α denotes the αth slip system.

The resolved shear stress, which plays a vital role in promoting slip, has been derived from the Cauchy stress tensor by the standard relationship.

$$\tau^{(\alpha)} = \boldsymbol{\sigma}\colon (\mathbf{s}^{(\alpha)} \otimes \mathbf{m}^{(\alpha)})_{\mathrm{sym}} \tag{4}$$

It is important to note that the slip direction and the vector normal to the slip plane used in the previous equation are defined for the deformed configuration, not the reference configuration. The slip direction and normal vector for the deformed configuration can be expressed in terms of the reference configuration as follows:

Presented as Paper 1836 at the 49th AIAA/ASME/ASCE/AHS/ASC Structures, Structural Dynamics, and Materials Conference, Schaumburg, Illinois, 7–10 April 2008; received 3 July 2008; revision received 12 June 2009; accepted for publication 16 June 2009.

*Graduate Research Assistant, Department of Mechanical and Aerospace Engineering; ctluo@asu.edu.

†Research Assistant Professor, Department of Mechanical and Aerospace Engineering; Jun.Wei.1@asu.edu. AIAA Member.

‡Graduate Research Assistant, Department of Mechanical and Aerospace Engineering; mparra2@asu.edu.

§Professor, Department of Mechanical and Aerospace Engineering; aditi@asu.edu. AIAA Fellow.

¶Associate Professor, Department of Mechanical and Aerospace Engineering; pperalta@asu.edu.

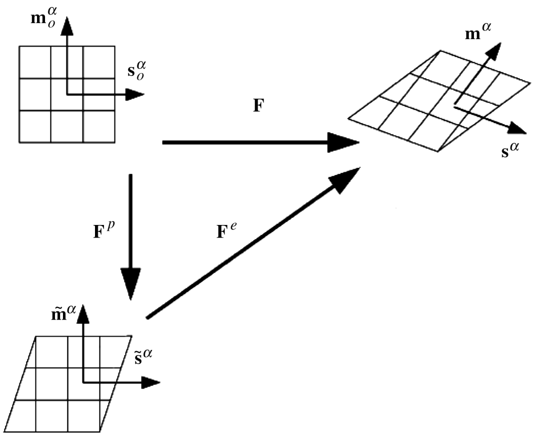

Fig. 1 Multiplicative decomposition of deformation gradient.

$$\mathbf{s}^{(\alpha)} = \mathbf{F}^{\mathbf{e}}\mathbf{s}_0^{(\alpha)} \quad \text{and} \quad \mathbf{m}^{(\alpha)} = \mathbf{m}_0^{(\alpha)}\mathbf{F}^{\mathbf{e}-1} \tag{5}$$

A power law is used in the flow rule to calculate the slip increments as follows [10,11]:

$$\dot{\gamma}^{(\alpha)} = \dot{\gamma}_0^{(\alpha)}\left|\frac{\tau^{(\alpha)} - \chi^{(\alpha)}}{g^{(\alpha)}}\right|^n \operatorname{sign}(\tau^{(\alpha)} - \chi^{(\alpha)}) \tag{6}$$

where $\dot{\gamma}_0^{(\alpha)}$ is the reference strain rate on slip system α, n is the strain rate exponent, and $g^{(\alpha)}$ and $\chi^{(\alpha)}$ represent the isotropic and kinematic hardening, respectively. Many research works have been done focusing on the hardening of single crystals including Taylor [3], Asaro [8], and Wu et al. [12]. They found that to describe the experimental observations which reflect different strain histories quantitatively, it is better to assume the evolution of the strengths $g^{(\alpha)}$ following the incremental relation

$$\dot{g}^{(\alpha)} = \sum_\beta h_{\alpha\beta}\dot{\gamma}^\beta \tag{7}$$

where Asaro [8] has used a simple form for the hardening moduli:

$$h_{\alpha\beta} = \begin{cases} h(\gamma) = h_0 \sec h^2 \left|\frac{h_0\gamma}{\tau_s - \tau_0}\right| & (\alpha = \beta) \\ qh(\gamma) & (\alpha \neq \beta) \end{cases} \cdot q$$

is material constant; h_0 is the initial hardening modulus; τ_s and τ_0 are the stage one stress and the yield stress, respectively. The cumulative shear strain on all slip systems can be obtained from $\gamma = \sum_\alpha \int_0^t |\dot{\gamma}^{(\alpha)}| \mathrm{d}t$. The details of hardening for crystalline materials can be found in Asaro's work [8,9,13]. The Armstrong—Frederick type kinematic hardening rule is used as

$$\dot{\chi}^{(\alpha)} = b\dot{\gamma}^{(\alpha)} - r\chi^{(\alpha)}|\dot{\gamma}^{(\alpha)}| \tag{8}$$

where b and r are material constants.

Numerical Results

A copper bar has been analyzed in ABAQUS using a user-developed implicit material subroutine (UMAT) code based on Huang's work [14]. To verify the constitutive model for fatigue analysis, the same material properties from [13] are used, listed in Table 1. The bottom and left edges of the foremost surface coincide with the crystal (−101) and (010) directions, respectively, and the loading direction is parallel to (101, shown in Fig. 2). Because copper consists of face-centered cubic (FCC) crystal structures, there are well-defined families of slip planes and slip directions, that is, $\{111\}\langle 110\rangle$. A single FCC crystal will contain 12 slip systems composed of four slip planes, each with three slip directions. The result from this model is presented in Fig. 3. Figure 4 shows the cyclic load condition (displacement control) and Fig. 3 shows the stress-strain response using single crystal plasticity theory. Two important aspects, cyclic hardening and saturation, are clearly exhibited in Fig. 3. The accumulated shear strain, which is directly related to the microdamage, has also been investigated. Figure 5 demonstrates that the accumulated shear strain increases with the number of cycles. This is an important parameter for fatigue damage studies and will be used in the fatigue damage criterion section to calculate the fatigue damage parameter.

B. Mesoscale Model (Multigrain Structure)

The single crystal plasticity theory applied at the microlevel can now be implemented at the mesolevel. The material that is interested in this research work is Al 2024. Thus, all the simulations in the rest of this paper are focused on this material. Relevant material parameters are shown in Table 2. The material hardening constants used in Asaro's hardening model are adopted from [8] (shown in Table 2). In the mesoscale model the original structure contained 547 grains, which is sufficient to be a representative volume element (RVE). To ensure computation efficiency, the original structure was reduced to a structure with 64 grains by combining smaller grains with larger or similar ones. The small grains were chosen using a heuristic approach based upon the relative size and orientation of nearby grains; this insures no significant effects were excluded. Each grain is a single crystal structure using the microscale analysis. The approach used in this model for fatigue simulation at the mesoscale is generalized by the following three steps.

First, electron backscattering diffraction (EBSD) scans (Fig. 6) are used to determine the crystal orientations in terms of three Euler angles $(\theta_1, \theta_2, \theta_3)$. The following rotation matrix relates the Euler angles to the crystal axes of each grain, which are parallel to the global axes.

$$\begin{pmatrix} \cos(\theta_3)\sin(\theta_1) + \cos(\theta_1)\cos(\theta_2)\sin(\theta_3) & \cos(\theta_1)\cos(\theta_2)\cos(\theta_3) - \sin(\theta_1)\sin(\theta_3) & -\cos(\theta_1)\sin(\theta_2) \\ -\cos(\theta_1)\cos(\theta_3) + \cos(\theta_2)\sin(\theta_1)\sin(\theta_3) & \cos(\theta_2)\cos(\theta_3)\sin(\theta_1) + \cos(\theta_1)\sin(\theta_3) & -\sin(\theta_1)\sin(\theta_2) \\ \sin(\theta_2)\sin(\theta_3) & \cos(\theta_3)\sin(\theta_2) & \cos(\theta_2) \end{pmatrix} \tag{9}$$

The rows of the matrix are unit vectors describing the crystallographic axes parallel to the global XYZ axes; therefore, this is the rotation matrix from local axes to global axes.

Second, the software package OOF (object-oriented finite element analysis from the National Institute of Standards and Technology) is used to create and mesh the mesoscale structure from the EBSD scan (Fig. 7). Grains are represented by various colors and each has the same material but different crystal orientation.

Third, the commercial finite element analysis (FEA) software ABAQUS and the previously developed UMAT are used to obtain stress distributions and the stress-strain response for any grain, as shown in Fig. 8. The specimen is tested under cyclic displacement control by applying displacement at the right edge of the mesoscale

Table 1 Material properties used in copper FCC structure

Elastic moduli	$C_{11} = 168.4$ GPa	$C_{12} = 121.4$ GPa	$C_{44} = 75.4$ GPa	
Material constants in power law	$n = 10$	$\dot{\gamma}_0 = 0.001\ \mathrm{sec}^{-1}$		
Material constants in self and latent hardening	$h_0 = 541.5$ MPa	$\tau_s = 109.5$ MPa	$\tau_0 = 60.8$ MPa	$q = 1.0$

Table 2 Material properties used for Al 2024

Elastic moduli (GPa)	$D_{1111} = 112$, $D_{1122} = 59.5$, $D_{2222} = 114$, $D_{1133} = 59$, $D_{2233} = 57.5$, $D_{3333} = 114$, $D_{1112} = 1.67$ $D_{2212} = -0.574$, $D_{3312} = -1.09$, $D_{1212} = 26.7$, $D_{1113} = 1.25$, $D_{2213} = -0.125$, $D_{3313} = -1.12$ $D_{1213} = -1.92$, $D_{1313} = 26.2$, $D_{1123} = -1.92$, $D_{2223} = 1.86$, $D_{3323} = 0.068$, $D_{1223} = -0.125$ $D_{1323} = -1.09$, $D_{2323} = 24.7$			
Material constants in power law	$n = 10$	$\dot{\gamma}_0 = 0.001\ \mathrm{sec}^{-1}$		
Material constants in self and latent hardening	$h_0 = 8.9\tau_0$	$\tau_s = 1.8\tau_0$	$\tau_0 = 76$ MPa	$q = 1.0$

structure. In Fig. 8a, the cool colored grains (green and cooler) are still under elastic deformation while the warm colored grains (yellow and red) already undergo plastic deformation. This indicates that material has an anisotropic, heterogeneous response at the grain level due to different crystal orientations and grain shapes. The stress-strain response of two adjacent grains is presented in Fig. 8b. From the plots, these two adjacent grains exhibit different material behaviors. The one in red has higher stress but lower strain compared with the other one. This again makes it clear that the model used can capture the orientation effects on material behavior at the grain level.

Numerical Results:

In the numerical study, the effect of microvoids/microcracks on material stiffness is investigated. Using the procedures previously described, a mesoscale structure containing nine microvoids, three of which are shown in Fig. 9 (circled), is analyzed. In this analysis,

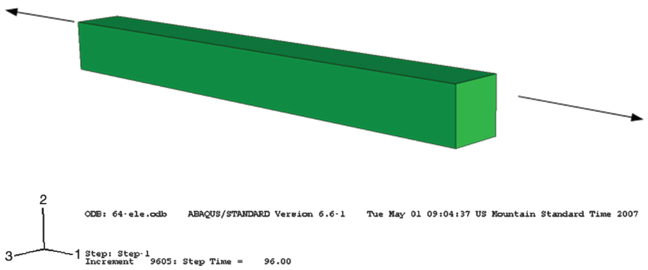

Fig. 2 Crystal orientation and loading direction.

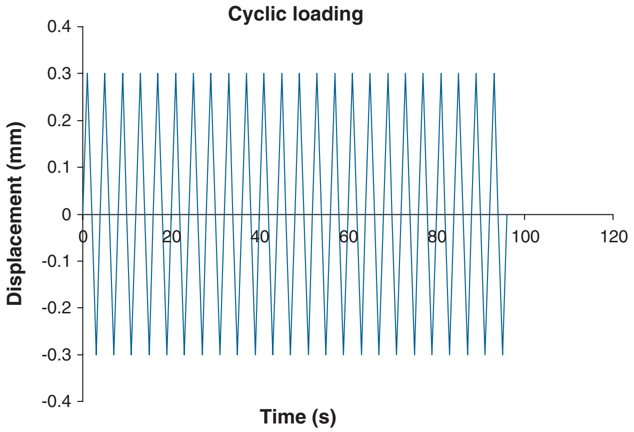

Fig. 3 Cyclic loading condition.

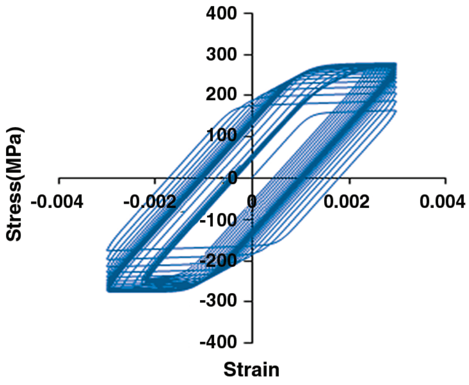

Fig. 4 Stress-strain response.

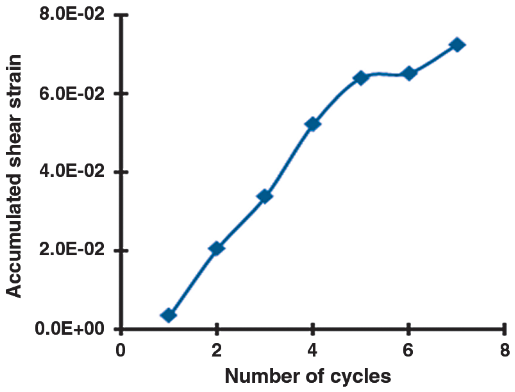

Fig. 5 Accumulated shear strain variation with number of cycles.

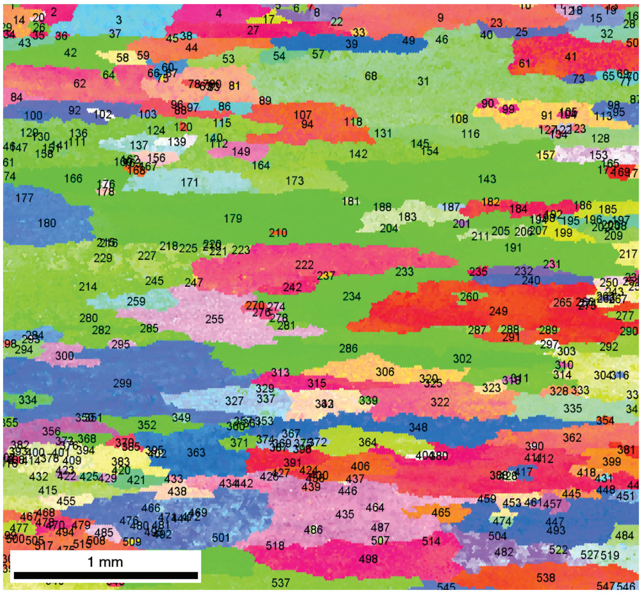

Fig. 6 EBSD scan of Al 2024 microstructure.

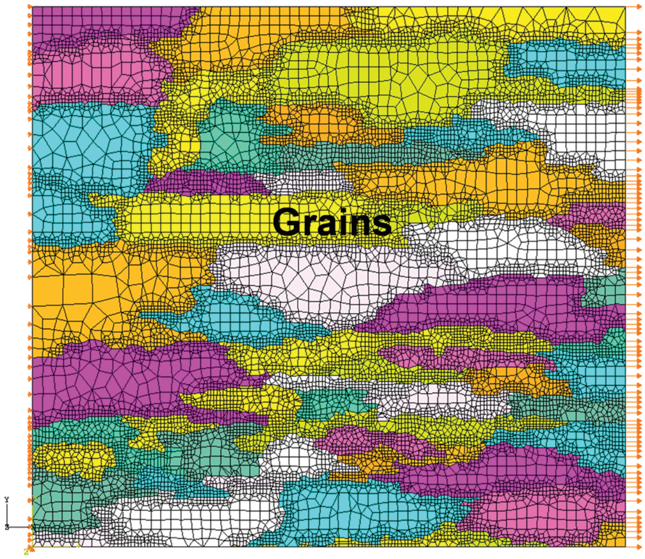

Fig. 7 Finite element model of Al 2024 microstructure.

fatigue loading is not considered; instead static loading is applied along the right edge. The comparison of the stress-strain curves along the loading direction is presented in Fig. 10, where the blue curve represents the undamaged structure and the purple curve represents the structure with the cracks (shown in Fig. 9).

The slopes of the elastic component in the two stress-strain curves shown in Fig. 10 are calculated. The stiffness drops by about 0.87% compared with the undamaged structure. Note that this reduction, although very small, represents a condition where the area ratio between microcracks and the mesoscale structure is only 0.2%. This can imply that the crack may cause a significant reduction in material stiffness as the area ratio increases. In addition, a small reduction in stress of 0.97% is observed in the structure with the cracks when the total strain reaches a value of 0.9%.

To further verify that the reduction is meaningful (and not caused by numerical noise), a second example is considered. A comparison of material behavior between an undamaged microstructure and the same microstructure with a single void inside is made. This time, the area fraction of the void is 1.59%. Figures 11 and 12 show the undamaged structure and the microstructure with a void, respectively. The comparison of the stress-strain response for the two microstructures is shown in Fig. 13. The stiffness decreases by 1.60% in the structure with the void compared with the undamaged structure. The maximum numerical error caused by linear fitting is 0.28%, which means that the reduction cannot be caused by data fitting. To compare Figs. 8a and 9, the result indicates that in a microstructure with cracks, the defects as well as crystal orientations affect the stress distribution. This conclusion is also supported by comparing the differences of stress distributions shown in Figs. 11 and 12. The

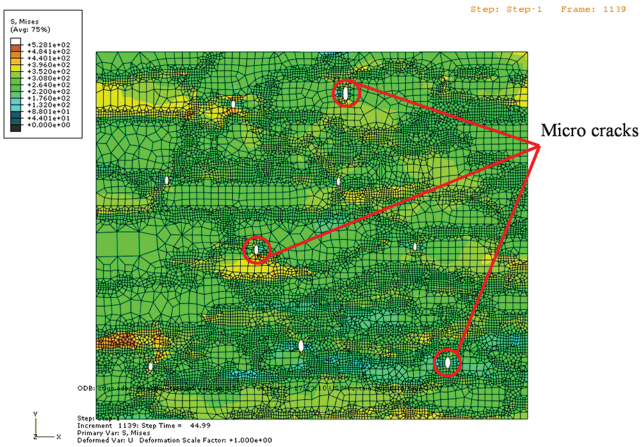

Fig. 9 Mises stress distribution of the microstructure with voids.

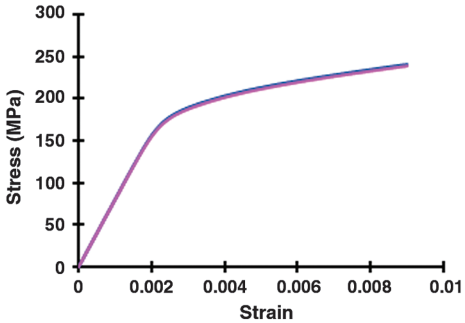

Fig. 10 Comparison of stress-strain response between undamaged microstructure (blue curve) and microstructure with voids (purple curve).

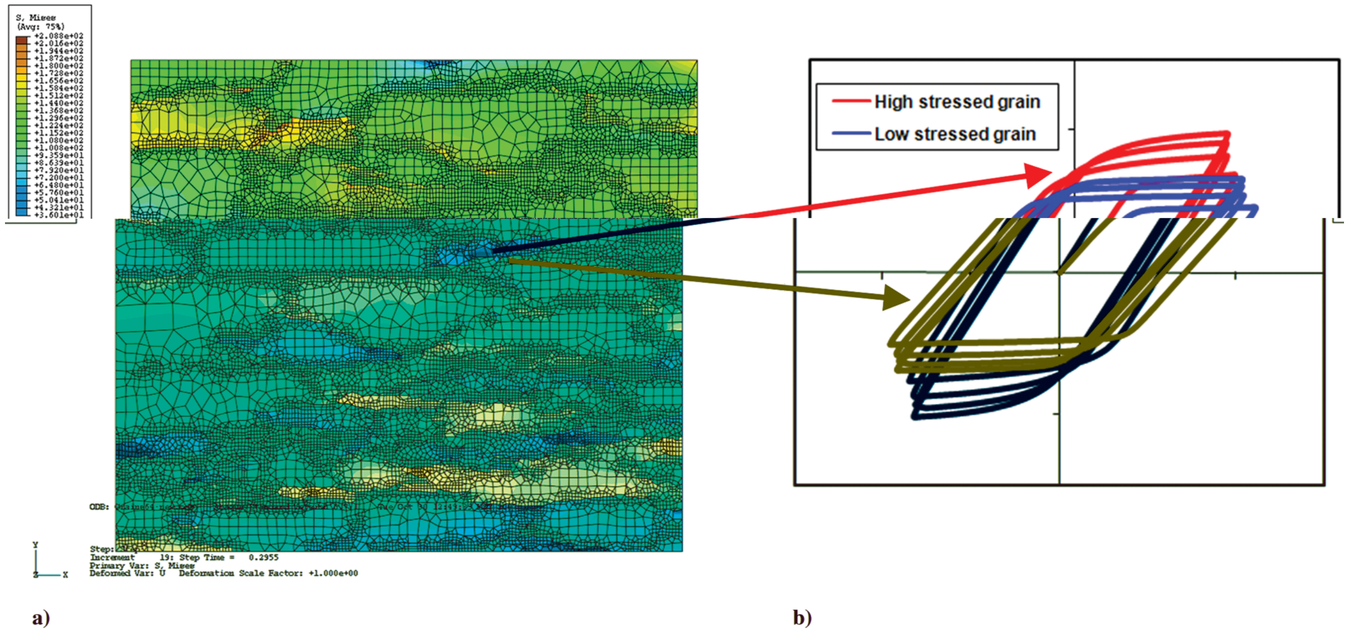

Fig. 8 a) Mises stress distribution in the RVE, and b) stress-strain response in different grains.

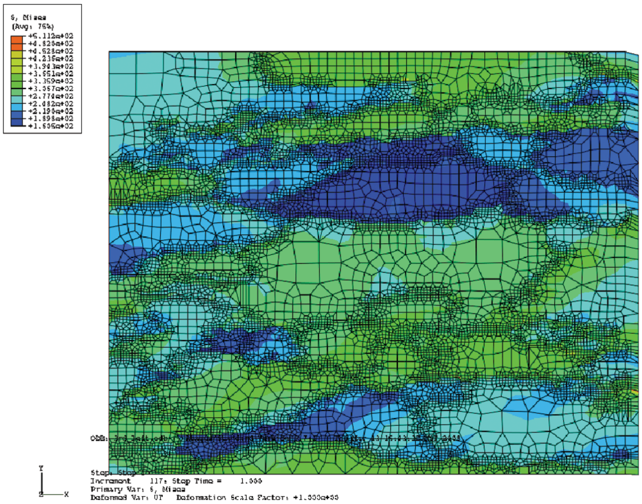

Fig. 11 Undamaged microstructure.

crystal orientations cause variations in the material behavior of each grain. Meanwhile, the microcrack causes stress concentrations at the crack tip (shown in the zoomed-in image in Fig. 12). Such phenomena will be help to understand how cracks initiate at the microstructure and propagate through the length scales to the meso and macrolevels.

However, the two examples are not comparable because they are based on different undamaged structures. To investigate the effect of microvoid distribution and to confirm that the existence of microvoids in the microstructure do cause the material stiffness degradation, more simulations are conducted based on one undamaged structure. The results are shown in Table 3. Corresponding structures for simulation case 1–case 5 in Table 3 are presented in Fig. 14. For case 2 and case 4, the shape and location of the single voids are approximately the same. The same condition is used for case 3 and case 5. Case 2 and case 3 used the same void area fraction. Similarly, case 4 and case 5 are created under the same void area fraction. Two points can be concluded from the results shown in Table 3. First, it is clear that under the same area fraction, the single crack is more harmful than distributed microvoids due to more degradation on elastic stiffness. Secondly, the more void area fraction the structure has, the more elastic stiffness degradation is caused.

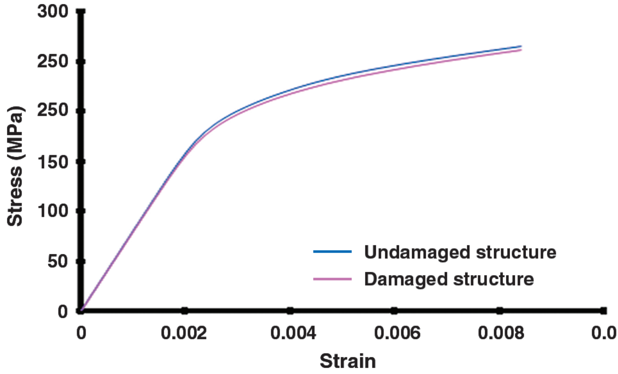

Fig. 13 Comparison of stress-strain response between undamaged microstructure and microstructure with a single void.

C. Applications and Validation at Macroscale

The results shown in the previous section demonstrate that the grain information including grain shape, size, and orientation from the microscale are still considered at the mesoscale. However, as far as applications at macroscale are concerned, to use the mesoscale model directly is not an efficient option. Besides, to validate the micro–meso model, data from experiments performed at microscale are needed. It is not available for us currently. To apply this model to do structural analysis at the macroscale, an averaging method has been employed. The validation is then carried out at macroscale. Assuming that the mesoscale structure containing 64 grains is a representative volume element (RVE), the average stress-strain response is calculated in ABAQUS (Fig. 15).

Numerical Results

Using this constitutive relation, two components have been analyzed: a notched dogbone (Fig. 16) and a lug joint (Fig. 17). The ratio between the length and width of the dogbone is 4:1. Figure 17a shows the dimensions of the lug joint specimen. Both Figs. 16 and

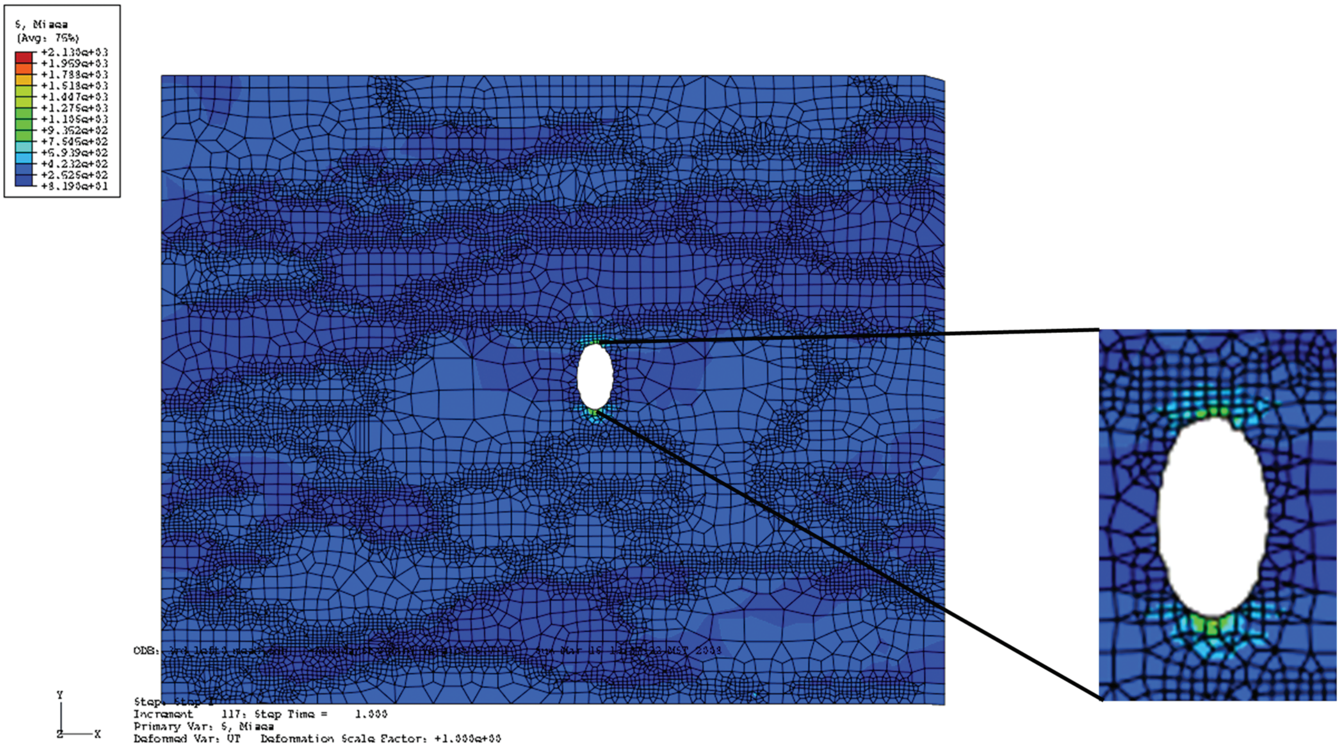

Fig. 12 Microstructure with a single void.

Table 3 Comparison of elastic stiffness for different damaged structures

Simulation	Microvoid type	Void area fraction	Elastic stiffness, GPa
Case 1	No void	0%	80.06
Case 2	Single void	0.901%	77.30
Case 3	Multiple voids	0.901%	77.50
Case 4	Single void	1.271%	76.24
Case 5	Multiple voids	1.271%	76.34

17b show the material degradation zones of the samples under uniaxial tension. The material degradation zones are calculated based on changes of plastic strain energy density. The instantaneous modulus E_t under unidirectional load is defined as $E_t = (1 - d)E_0$, where E_0 is the initial modulus of 73 GPa, and d is the damage factor described as d=W t/W c, and where w_c is the critical plastic strain energy density of 3.94 MPa calculated from the monotonic tension stress-strain curve of Al 2024 [15], and w_t is the instantaneous plastic strain energy density.

The yield strength of the material is 149 MPa and Poison's ratio is 0.33. Both the initial modulus and yield strength are calculated from the average stress-strain curve (shown in Fig. 15). In the dogbone specimen there exists a very sharp material degradation zone around the notch and in the lug joint specimen there exist two sharp material degradation zones at the shoulder of the specimen. Because of symmetric condition, half of the lug joint was analyzed in ABAQUS. Figure 18 shows the finite element (FE) model of the lug joint and Fig. 19 shows the Mises stress distribution in the lug joint. From the stress distribution, we calculated the energy release rate versus crack length (shown in Fig. 20). The estimated critical crack length at which the crack growth will be unstable is 8 mm derived from Fig. 20. Experiments were carried on lug joints under fatigue loading [16]. The critical crack length obtained was 7.53 mm (Fig. 21) and the estimated critical crack length is in agreement with the experimental result.

III. Fatigue Damage Criterion

Fatigue damage is a common effect of cyclic loading that engineering components are often subjected to. Thus, it is important and necessary to understand and characterize the behavior of a structure under cyclic loading. Usually crack growth and its propagation direction are considered separately with different criteria. Meanwhile, most damage criteria can only be applied at the macroscale. In this section, a comprehensive fatigue damage criterion is proposed that can predict the crack growth rate and cracking direction simultaneously. The criterion, which is available in literature [17], is expressed as follows:

$$dD = \langle \sigma_{mr} - \sigma_0 \rangle^m \left(1 + \frac{\sigma}{\sigma_f}\right) dY \tag{10}$$

where

$$dY = \alpha \sigma d\varepsilon^p + \frac{1-\alpha}{2} \tau d\gamma^p \tag{11}$$

σ is the normal stress and τ is the shear stress on a material plane. The quantities ε^p and γ^p represent plastic strains corresponding to σ and τ, respectively, and α and m are material constants. The symbol $\langle\,\rangle$ denotes the MacCauley bracket and σ_f is the true fracture stress of the material. The quantity σ_{mr} is a material memory parameter and Y is the plastic strain energy on a material plane. The memory stress introduced here equals the maximum Mises equivalent stress in the principal deviatoric stress space. This fatigue model implies that the plastic strain energy on a material plane, Y, is the major cause of fatigue damage.

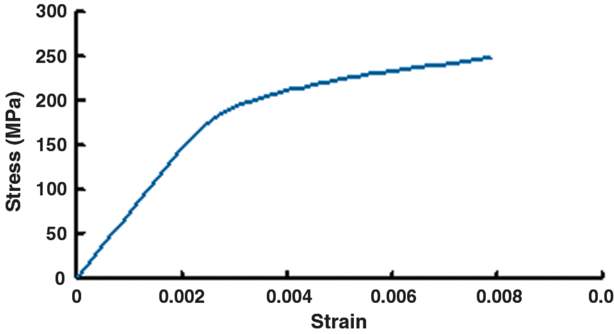

Fig. 15 Average stress-strain response of the RVE.

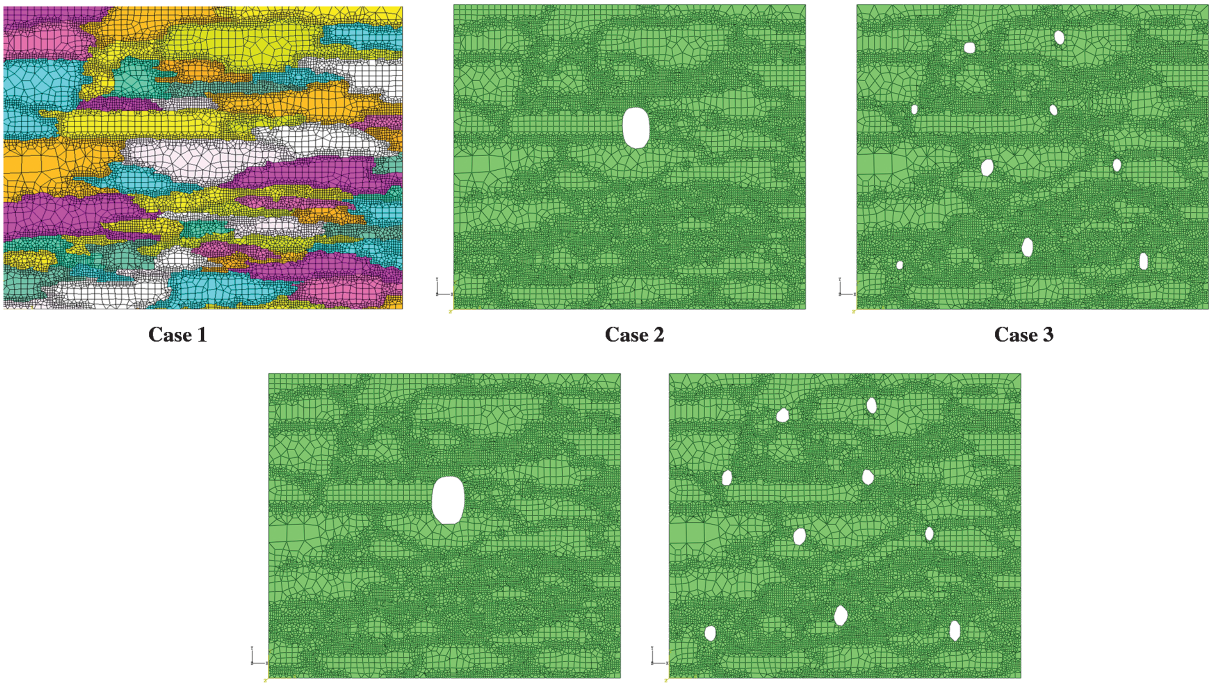
Case 1

Case 2

Case 3

Case 4

Case 5

Fig. 14 Case 1, undamaged microstructure, and cases 2–5, microstructure with void/voids.

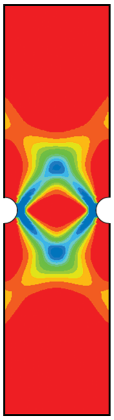

Fig. 16 Material degradation area in dogbone.

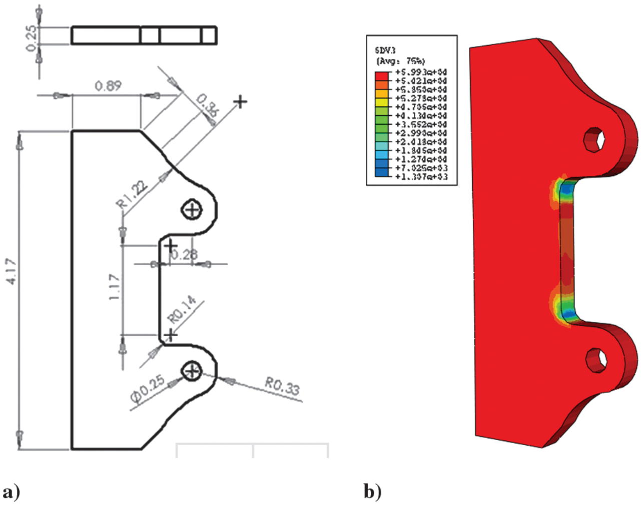

Fig. 17 a) Geometrical dimensions of the lug joint sample, and b) material degradation area in the lug joint.

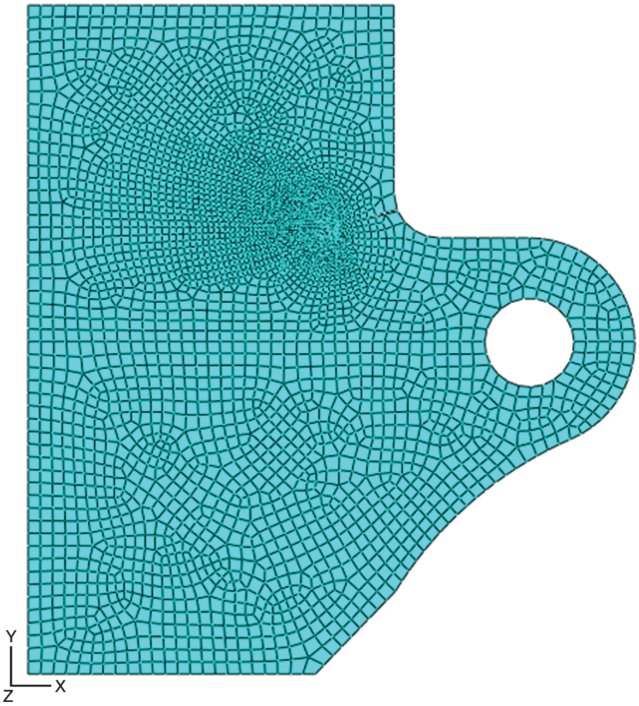

Fig. 18 Finite element mesh of the symmetric part of the lug joint.

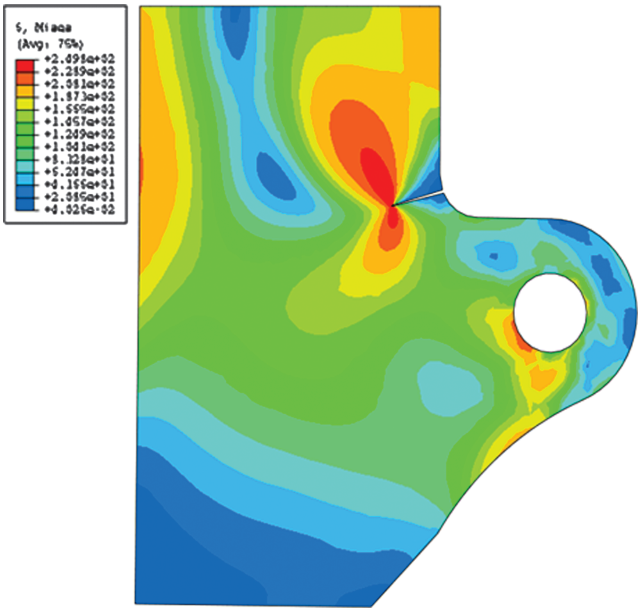

Fig. 19 Mises stress distribution in the symmetric part of the lug joint.

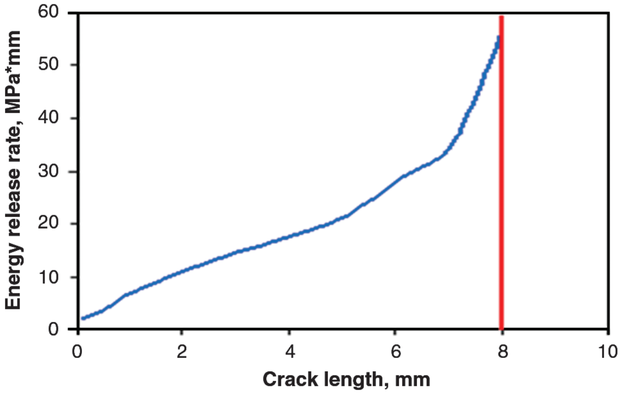

Fig. 20 Energy release rate vs crack length.

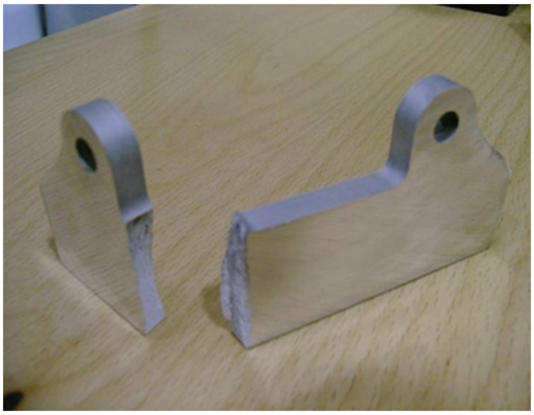

Fig. 21 Failure location of the polished lug joint sample tested under a constant amplitude loading of 110–1100 lb.

To decide the damage growth rate and cracking direction, the accumulated fatigue damage should be calculated along all the directions in 3D space. Next, the critical material plane where the maximum accumulated fatigue damage reaches a critical value needs to be determined; the direction of crack propagation is along the critical material plane [17,18]. It is quite elegant that this model can be used to predict fatigue damage growth well under multiaxial loading and nonproportional loading. It also has the capability to

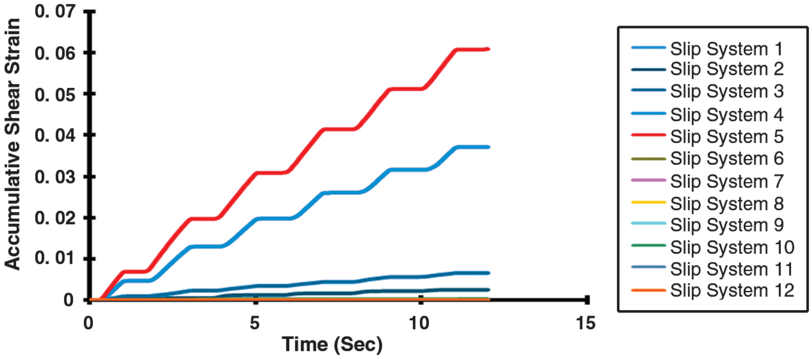

Fig. 22 Accumulative shear strain in 12 slip systems.

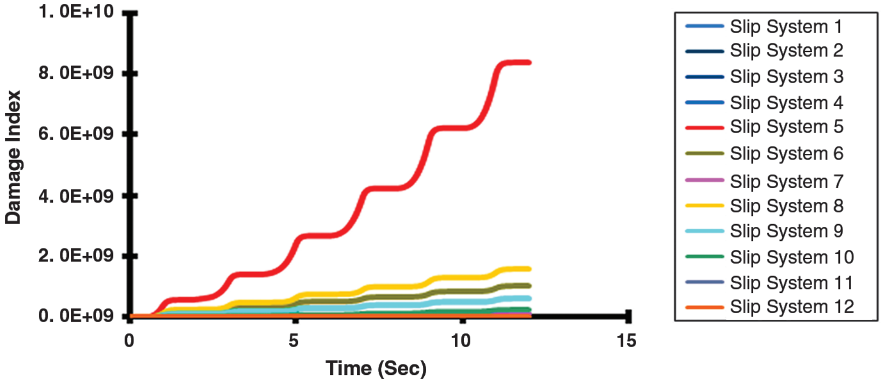

Fig. 23 Fatigue damage evolution in 12 slip systems.

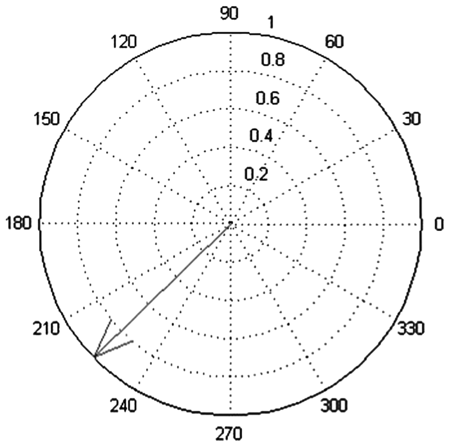

Fig. 24 *X-Y* plane projection of the normal to the critical slip plane.

track fatigue crack grow under changing loading direction [18]. However, this method is computationally expensive and time inefficient to implement in 3D. Experimental observations indicate that fatigue cracks at the microscale always nucleate along slip planes; therefore, the incorporation of single crystal plasticity makes it reasonable to assume that the critical material plane will be one of the activated slip systems. The corresponding criterion should be rewritten as:

Table 4 Normal and slip direction of the critical slip system

	Normal to the slip plane	Slip direction in the slip plane
X coordinate	−0.713215	−0.662362
Y coordinate	−0.693905	0.620869
Z coordinate	0.0991835	−0.41925

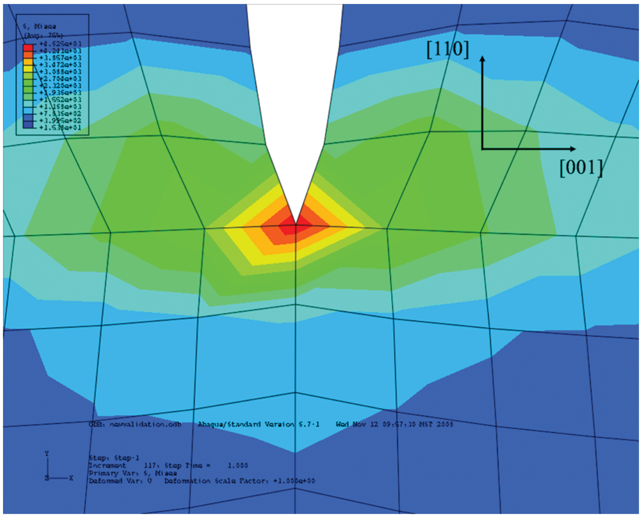

Fig. 25 Mises stress distribution in a precracked single crystal plate under uniaxial tensile loading.

$$dD = \langle \sigma_{mr} - \sigma_0 \rangle^m \left(1 + \frac{\sigma^{(\beta)}}{\sigma_f} \right) dY \tag{12}$$

$$dY = \alpha \sigma^{(\beta)} d\varepsilon^{p^{(\beta)}} + \frac{1-\alpha}{2} \tau^{(\beta)} d\gamma^{p^{(\beta)}} \tag{13}$$

where β denotes the βth slip system. Unlike the criterion from [19], which considered all three slip systems within the same slip plane together, the slip systems are considered separately in this research work. This procedure is used as the first step to construct a damage tensor at the microscale in the author's later work [20]. Compared with the original model, the computational efficiency is improved by

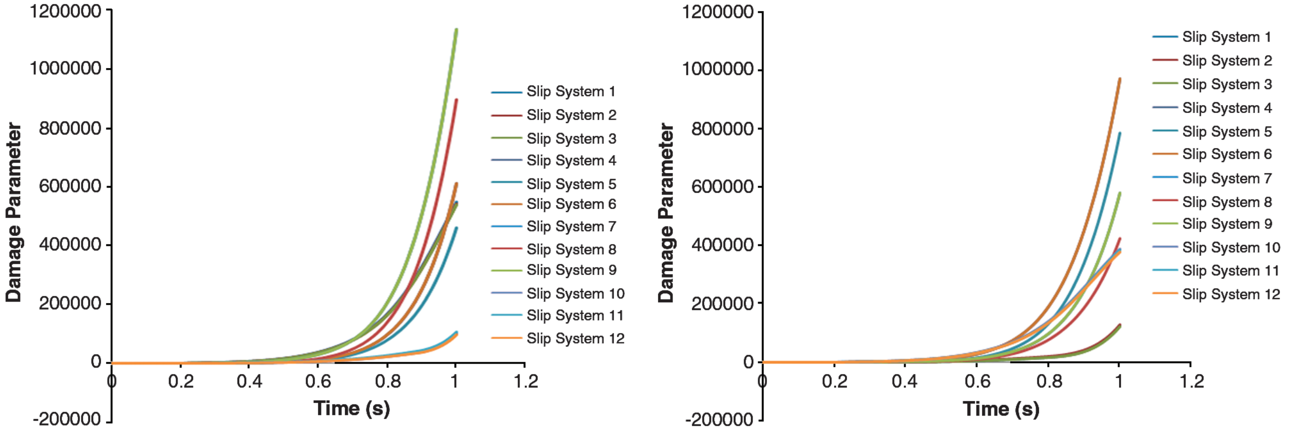

a) b)

Fig. 26 a) Damage evolution for 12 slip systems on a) left-hand side of the crack tip, and b) right-hand side of the crack tip.

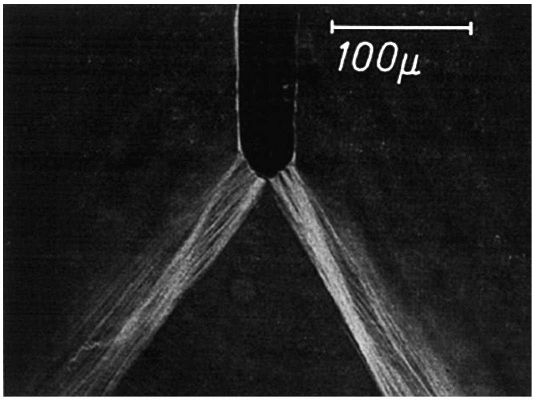

Fig. 27 Scanning electron microscope (SEM) micrograph showing the slip before the crack tip [20].

calculating damage parameter only among potential active slip systems instead of calculating accumulated fatigue damage along all the directions in 3D space. Once the accumulative damage parameter reaches a critical damage value, the material is regarded as failed. The corresponding damage index is defined as: $D_{\text{index}} = \frac{D_a}{D_c}$, where $D_a = \int_t dD\mathrm{d}t$ is the accumulative damage parameter at a certain point of the structure and D_c is the critical damage value. In the following numerical results part, the accumulative damage parameters within 12 potential active slip systems are only presented. The determination of the critical damage value can be found in the author's later work [20].

Numerical Results

Cyclic loading is applied at the right edge of the mesoscale structure, which has been used in Sec. II.B. Figure 22 shows the accumulative shear strain in each slip system in the element where the maximum damage was obtained. The fatigue damage evolution at different slip systems in the same element is presented in Fig. 23. The flat part of the curve indicates the unloading portion of a cycle. Comparing these two figures, a unique slip system (slip system 5) is prevalent with respect to the others and this will be considered as the dominant slip system. Slip system 5 is the maximum shear-strain plane and also has the highest damage value; this also agrees with the findings of Lemaitre [2]. Figures 22 and 23 indicate that the slip plane for maximum shear strain is the same for maximum damage parameter. However, this behavior is not exhibited by other slip planes due to the influence of normal stress on damage parameter. Table 4 lists the normal and slip direction of the slip system. The Z coordinate of normal is very small compared with the X and Y coordinates. That means the slip plane almost lies in the X-Y plane. The X-Y plane projection of normal is shown in Fig. 24. It shows that the critical slip plane is approximately 45° to the loading direction.

To further confirm that this model can predict the critical slip system and then determine the critical material plane, another example is conducted. This example shown in Fig. 25 is very similar to the push–pull specimen from [21]. Using the same procedures described in the previous section, the damage accumulation within 12 potential active slip systems for the left-hand-side and right-hand-side elements just in front of the crack tip are investigated. Figures 26a and 26b show the damage evolution in 12 slip systems of the left-hand-side and right-hand-side elements, respectively. From the two plots, two critical slip systems are determined. One is on the left-hand side and one is one the right-hand side. The corresponding global coordinates of the normal to the critical slip plane for the left-hand side is [0.57735, 0.816497, 0] and the corresponding global coordinates of the normal to the critical slip plane for the right-hand side is $[0.57735 \quad -0.816497 \quad 0]$. This is in accordance with the experimentally observed results in Fig. 27 cited from [21].

IV. Conclusions

A multiscale model was used to address the problem of predicting fatigue damage accumulation in metallic materials. Single crystal plasticity served as the foundation for the mesoscale modelling, applied to each grain. The results reveal that different crystal orientations will cause an anisotropic behavior at the mesoscale. Macroscale analysis was accomplished by using the average stress-strain response from the mesoscale. Macroscale effects were investigated by determining the material degradation zones for two types of specimens, a dogbone sample and lug joint, under uniaxial loading. Using the developed multiscale model, a fatigue damage criterion was modified for single crystal plasticity. Under uniaxial loading condition, results indicate that for a given critical value of accumulated damage parameter, the probability of failure to occur is approximately at 45° plane relative to the loading direction.

Acknowledgments

This research is supported by the U.S. Department of Defense, U.S. Air Force Office of Scientific Research Multidisciplinary University Research Initiation Grant, FA95550-06-1-0309, Technical Monitor Victor Giurgiutiu.

References

[1] United States Air Force Scientific Advisory Board, "Report of the AdHoc Committee on Air Force Aircraft Jet Engine Manufacturing and SAF/AQQS," the Pentagon, Washington, D.C, 1992.

[2] Lemaitre, J., and Desmorat, R., *Engineering Damage Mechanics*, Springer–Verlag, New York, 2005.

[3] Taylor, G. I., "Plastic Strain in Metals," *Journal of the Institute of Metals*, Vol. 62, 1938, pp. 307.

[4] Hill, R., "Generalized Constitutive Relations for Incremental Deformation of Metal Crystals by Multislip," *Journal of the Mechanics and Physics of Solids*, Vol. 14, No. 2, 1966, pp. 95–102.

doi:10.1016/0022-5096(66)90040-8

[5] Rice, J. R., "Inelastic Constitutive Relations for Solids: An Internal-Variable Theory and its Application to Metal Plasticity," *Journal of the Mechanics and Physics of Solids*, Vol. 19, No. 6, 1971, pp. 433–455. doi:10.1016/0022-5096(71)90010-X

[6] Hill, R., and Rice, J. R., "Constitutive Analysis of Elastic–Plastic Crystals at Arbitrary Strain," *Journal of the Mechanics and Physics of Solids*, Vol. 20, No. 6, 1972, pp. 401–413. doi:10.1016/0022-5096(72)90017-8

[7] Asaro, R. J., and Rice, J. R., "Strain Localization in Ductile Single Crystals," *Journal of the Mechanics and Physics of Solids*, Vol. 25, No. 5, 1977, pp. 309–338. doi:10.1016/0022-5096(77)90001-1

[8] Asaro, R. J., "Micromechanics of Crystals and Polycrystals," *Advances in Applied Mechanics*, Vol. 23, 1983, pp. 1–115. doi:10.1016/S0065-2156(08)70242-4

[9] Asaro, R. J., "Crystal Plasticity," *Journal of Applied Mechanics*, Vol. 50, No. 4B, 1983, pp. 921–934. doi:10.1115/1.3167205

[10] Horstemeyer, M. F., McDowell, D. L., and McGinty, R. D., "Design of Experiments for Constitutive Model Selection: Application to Polycrystal Elastoplasticity," *Modelling and Simulation in Materials Science Engineering.*, Vol. 7, No. 2, 1999, pp. 253–273.

[11] Horstemeyer, M. F., and McDowell, D. L., "Modeling Effects of Dislocation Substructure in Polycrystal Elastoplasticity," *Mechanics of Materials*, Vol. 27, No. 3, 1998, pp. 145–163. doi:10.1016/S0167-6636(97)00037-9

[12] Wu, T., Bassani, J. L., and Laird, C., "Latent Hardening in Single Crystals, Part I, Theory and Experiments," *Proceedings of the Royal Society of London A*, Vol. 435, No. 1893, 1991, pp. 1–19.

[13] Peirce, D., Asaro, R. J., and Needleman, A., "An Analysis of Nonuniform and Localized Deformation in Ductile Single Crystals," *Acta Metallurgica*, Vol. 30, No. 6, 1982, pp. 1087–1119. doi:10.1016/0001-6160(82)90005-0

[14] Huang, Y., "A User-Material Subroutine Incorporating Single Crystal Plastictiy in the ABAQUS Finite Element Program," Harvard University, Mech. Report 178, Division of Engineering and Applied Sciences, 1991.

[15] Berkovits, A., "Variation of the Cyclic Strain-Hardening Exponent in Advanced Aluminium Alloys," *International Journal of Fatigue*, Vol. 9, No. 4, 1987, pp. 229–232.

[16] Soni, S., Das, S., and Chattopadhyay, A, "Simulation of Damage-Features in a Lug Joint Using Guided Waves," *Journal of Intelligent Material Systems and Structures*, Vol. 20, No. 12, 2009, pp. 1451–1463.

[17] Jiang, Y., "A Fatigue Criterion for General Multiaxial Loading," *Fatigue and Fracture of Engineering Materials and Structure*, Vol. 23, No. 1, 2000, pp. 19–32.

[18] Ding, F., Zhao, T., and Jiang, Y., "A Study of Fatigue Crack Growth With Changing Loading Direction," *Engineering Fracture Mechanics*, Vol. 74, No. 13, 2007, pp. 2014–2029. doi:10.1016/j.engfracmech.2006.10.013

[19] Kalnaus, S., and Jiang, Y., "Fatigue Life Prediction of Copper Single Crystals Using a Critical Plane Approach," *Engineering Fracture Mechanics*, Vol. 73, No. 6, 2006, pp. 684–696. doi:10.1016/j.engfracmech.2005.11.003

[20] Luo, C., Parra–Garcia, M., Chattopadhyay, A., Peralta, P., and Wei, J., "A Multiscale Damage Criterion for Fatigue Life Prediction in Metallic Materials," *50th AIAA/ASME/ASCE/AHS/ASC Structures, Proc. Structural Dynamics and Materials Conference*, Palm Springs, CA, May 2009.

[21] Neumann, P., "New Experiments Concerning the Slip Processes at Propagating Fatigue Cracks-I," *Acta Metallurgica*, Vol. 22, No. 9, 1974, pp. 1155–1165. doi:10.1016/0001-6160(74)90071-6

A. Roy
Associate Editor